Performance evaluation of a sensorless adaptive optics multiphoton microscope

MARTIN SKORSETZ, PABLO ARTAL & JUAN M. BUENO
Laboratorio de Óptica, Instituto Universitario de Investigación en Óptica y Nanofísica, Universidad de Murcia, Murcia, Spain

Summary

A wavefront sensorless adaptive optics technique was combined with a custom-made multiphoton microscope to correct for specimen-induced aberrations. A liquid-crystal-on-silicon (LCoS) modulator was used to systematically generate Zernike modes during image recording. The performance of the instrument was evaluated in samples providing different nonlinear signals and the benefit of correcting higher order aberrations was always noticeable (in both contrast and resolution). The optimum aberration pattern was stable in time for the samples here involved. For a particular depth location within the sample, the wavefront to be precompensated was independent on the size of the imaged area (up to $\sim 360 \times 360 \ \mu m^2$). The mode combination optimizing the recorded image depended on the Zernike correction control sequence; however, the final images hardly differed. At deeper locations, a noticeable dominance of spherical aberration was found. The influence of other aberration terms was also compared to the effect of the spherical aberration.

Introduction

Multiphoton microscopy (MPM) is an imaging modality allowing large penetration depths and intrinsic optical sectioning of thick samples (Denk *et al.*, 1990; Campagnola *et al.*, 2001). However, as the light propagates inside the specimen it passes through regions with changing refractive indices before reaching the plane to be imaged. This induces aberrations that distort the focal spot and limit imaging performance, reducing signal level, contrast and resolution (Booth & Wilson, 2001; Sherman *et al.*, 2002; Girkin *et al.*, 2009).

Adaptive Optics (AO) has been used to overcome these limitations and improve MPM image quality (Albert *et al.*, 2000; Neil *et al.*, 2000; Booth & Wilson, 2001; Sherman *et al.*, 2002; Marsh *et al.*, 2003; Rueckel *et al.*, 2006; Débarre *et al.*, 2009;

Correspondence to: Juan M. Bueno, Laboratorio de Óptica, Instituto Universitario de Investigación en Óptica y Nanofísica, Universidad de Murcia, Campus de Espinardo (Ed. 34), 30100 Murcia, Spain. Tel: 34–868888335; fax: 34–868883528; e-mail: bueno@um.es

Bueno *et al.*, 2010). Due to the difficulty of a plane-by-plane aberration correction within the sample, the most extended scheme for AO-MPM is the so-called wavefront sensorless (WFSL) technique. In WFSL approaches, the adaptive element precompensates for the unknown sample's aberrations without measuring them. They use iterative algorithms such as genetic learning (Albert *et al.*, 2000; Sherman *et al.*, 2002; Wright *et al.*, 2005), hill-climbing/sequential (Neil *et al.*, 2000; Marsh *et al.*, 2003; Wright *et al.*, 2005; Débarre *et al.*, 2009), stochastic (Zhou *et al.*, 2011) or random search (Wright *et al.*, 2005; Tang *et al.*, 2012) to find the best image according to a predefined image quality metric.

Deformable mirrors have been the most widely used adaptive element in AO-MPM and the use of spatial light modulators (SLMs) has been less common (Neil *et al.*, 2000; Shao *et al.*, 2012), probably due to the fact that their reflectance is $\sim 50\%$ and they require incident linear polarized light. Although this low reflectance and polarization dependence might limit the imaging of deeper planes within the specimen, the use of Liquid-Crystal-on-Silicon (LCoS) devices has overcome these drawbacks. In particular, LCoS modulators have been reported to be suitable for MPM imaging at deep locations within the mouse cortex (Ji *et al.*, 2010, 2012).

AO-MPM experiments have reported image improvement in samples providing two-photon excitation fluorescence (TPEF) (Marsh *et al.*, 2003; Rueckel *et al.*, 2006; Débarre *et al.*, 2009; Bueno *et al.*, 2010; Ji *et al.*, 2010, 2012; Aviles-Espinosa *et al.*, 2011; Tao *et al.*, 2013) and third harmonic generation (Jesacher *et al.*, 2009; Olivier *et al.*, 2009). Although second harmonic generation (SHG) is another form of nonlinear microscopy, literature dealing with AO SHG image improvement is scarce (Jesacher *et al.*, 2009; Bueno *et al.*, 2010, 2014).

WFSL algorithms often use Zernike polynomials to express the WA. The individual Zernike modes are generated by the active element, starting with lower order modes and sequentially increasing the aberration order. Moreover, WFSL procedures determine the 'optimum' global wavefront aberration (WA) for each imaged plane within the sample. Because they do not take into account the variations of the aberrations across the field, the technique would be appropriate if aberrations are
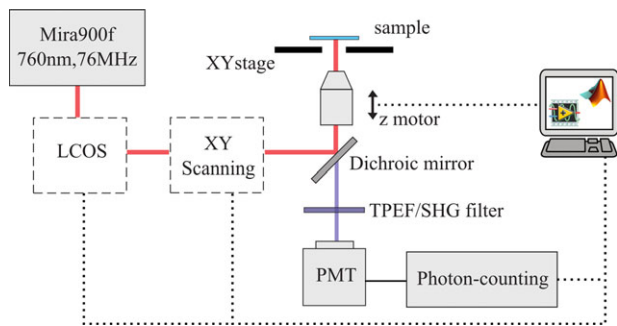
Fig. 1. Experimental setup: LCoS, liquid-crystal-on-silicon, PMT, photo-multiplier tube.

approximately constant across a microscope's field of view. This occurs when the imaged field is small, but not for larger imaged areas where aberrations can significantly vary across the image (Schwertner *et al.*, 2004; Hovhannisyan *et al.*, 2008; Simmonds & Booth, 2013; Zheng *et al.*, 2013).

We extend here the WFSL-MPM concept by means of an LCoS-SLM device used as adaptive element. Both TPEF and SHG images at different depth locations are optimized by using a hill-climbing algorithm. The performance of the instrument for different experimental and operational conditions is evaluated. The relationship between the order of the Zernike mode sequence correction and the final WA pattern is investigated. Furthermore, the stability in the correction as well as the dependence between the imaged area size and the corresponding optimum WA is also studied.

Methods

Experimental setup

Figure 1 depicts a schematic diagram of the experimental setup used in this work. This is a modified version of the research prototype AO multiphoton microscope previously described (Bueno *et al.*, 2010). A mode-locked Ti:Sapphire laser (760 nm) was combined with an inverted microscope, a XY scanning unit and a photomultiplier tube (PMT). A DC z-motor was used to change the imaged plane along the sample's depth. A dichroic mirror separated the incident light from the two backscattered nonlinear signals emitted by the specimens, TPEF and SHG. TPEF/SHG spectral filters placed in front of the PMT separated both signals. Because future applications of this setup will be centred on imaging *in vivo* ocular tissues (where immersion media are not comfortable for the subjects), an in-air long-working distance objective (20x, NA = 0.5) was chosen.

The collimated laser beam was spatially modulated by an LCoS-SLM (Pluto IR 2 Holoeye, Berlin, Germany) optically conjugated with the entrance pupil of the microscope objective. This beam was linearly polarized along the active axis of the LCoS-SLM. Details on calibration and phase mask wrapping

operation can be found elsewhere (Fernández *et al.*, 2009). This device has 1920×1080 pixel resolution (8.0-μm pixel pitch) and was specifically designed to provide a phase shift above 2π for the used wavelength (i.e. optimized for infrared light).

Procedure

The AO optimization procedure consisted of a WFSL technique based on a hill-climbing algorithm (Marsh *et al.*, 2003). This is an iterative searching technique looking for the WA map producing an image with the highest metric value. The WA was expressed as an expansion in Zernike polynomials. The individual Zernike modes are sequentially generated by the LCoS-SLM, ranging from 2nd (except defocus) to 4th order. The algorithm was run over 11 Zernike terms in total. The usual hill-climbing procedure corrects for Zernike modes in the 'increasing-mode direction', that is, it starts with 2nd-order terms and goes through 3rd and 4th order ones. However, for comparisons, the procedure was also performed here in the 'decreasing-mode direction'; that is, starting with 4th-order terms in reverse order. Along this work, the Zernike modes are described using the OSA double-index convention (subindex and superindex indicate the order and the frequency respectively).

For every Zernike term, its amplitude (both positive and negative) was changed in predefined steps until the recorded image provided the maximum metrics value. An example of this is shown in Figure 2. Once this value is set, the procedure is repeated again for the next Zernike mode. If the Zernike mode control sequence is run in the increasing order, the final WA is estimated when the optimum amplitude of the term $Z_4{}^4$ is obtained. In the decreasing-order direction, the term $Z_4{}^0$ (spherical aberration) was the first one (see Results section for details on this). For a better understanding, a schematic diagram of the algorithm is depicted in Figure 3. Image acquisition, AO correction and image processing were done through custom software written in LabView™ (Austin, TX, USA) and MatLab™ (The MathWorks, Inc, Natick, MA, USA). The total time for the entire procedure was about 3 min.

The chosen image quality metric to be maximized was the image sharpness (Muller & Buffington, 1974), defined as:

$$M = \int \int I(x, y)^2 dx \cdot dy. \tag{1}$$

This metric has been reported to take a maximum value only when the WA produced by the LCoS-SLM cancels out the combined WA of the optical system and the sample.

Samples

As non-biological samples, pieces of stained cellulose and silk mesh were used to provide TPEF signal. As biological specimens, different non-stained ocular tissues were imaged: human epiretinal membrane, rat retina and bovine
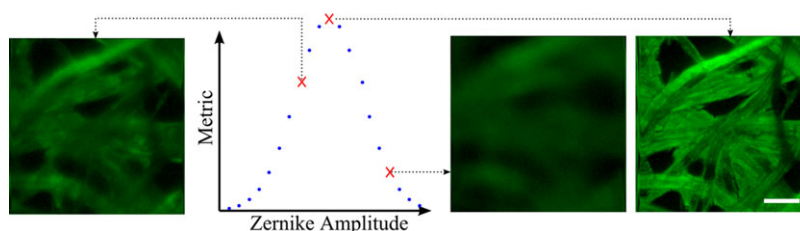
Fig. 2. Illustrative example of image improvement (piece of cellulose) using the hill-climbing modal optimization algorithm for an individual Zernike term. Images correspond to the Zernike amplitude and metric value marked on red. Bar length: 50 μm.
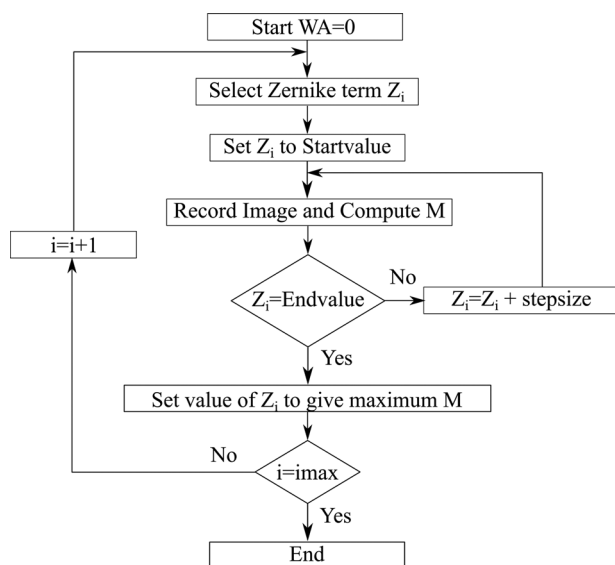

Fig. 3. Flow chart of the algorithm used to optimize images recorded with WFSL MPM.

sclera (fixed in paraformaldehyde), non-stained rabbit and bovine corneas (embedded in paraffin wax). Whereas the two former ones provide TPEF signal, the rest emits SHG (Han *et al.*, 2005; Bueno, Gualda, & Artal, 2011; Bueno, Gualda, Giakoumaki *et al.*, 2011). Samples embedded in paraffin are thin histological sections, with reduced transparency and maximum thickness of about 40 μm. For a better discrimination, TPEF and SHG images are displayed in green and blue (false colours), respectively.

Results

Image improvement of a single plane

In order to evaluate the robustness of the LCoS-SLM and the performance of the proposed algorithm, multiphoton images were first optimized for different samples at a single plane. The image plane was randomly selected by the operator. Figure 4 shows MPM images for different samples before and after AO correction. The insets represent the precompensated WAs. The intensity profiles correspond to the lines indicated in the images.

The WFSL procedure improved the images corresponding to both nonlinear imaging modalities, independently of their nature. However, as expected, the WA producing the optimum image according to the chosen metric differed among samples. Moreover, there is an increase in both contrast and resolution (small features not present in original images appeared in the images when using AO). For these particular examples, the WA root-mean-square (RMS) values were respectively 1.05, 0.46 and 0.40 μm. The increase in signal (total intensity, that is, summation of all pixels across the image) was higher than 2-fold for these specimens in comparison to the uncorrected image.

As an additional example, the increase in contrast and resolution at a particular depth is shown in Figure 5 when visualizing 'SHG natural beads' within a rabbit cornea. At 0-μm position, the beads are easily observed and the AO operation has no effect (i.e. the images before and after WA compensation are the same). However, these beads are hardly seen when imaging a plane at 50-μm depth. When the WFSL algorithm is used, the increase in image quality (and associated parameters) is noticeable (see differences in colour bars of bottom images). It can also be observed how before using AO, a 'large' and 'defocused' spot appears at the top right side of image acquired at 50 μm. When AO is in operation, this spot turns into 'two beads' due to the increase in resolution.

Although all the specimens used are static samples, experimental conditions may vary due to uncontrolled changes (laser stability, thermal effects, photo-damage). The temporal stability of the procedure has been tested in two samples. Figure 6 shows pairs of images before and after AO operation recorded some hours apart (24 and 8 h for TPEF and SHG images, respectively). Final improved images are similar and the corresponding WAs hardly changed with time. Differences between RMS values were smaller than 5% and the Zernike distribution were similar (see plot on the right of Fig. 6).

Influence of the imaged area

As spatial features within the sample might be very different across the imaged area, the WA able to optimize the image might depend on the visual field. Now the question would be: To what extent can a WA correction for a particular area be
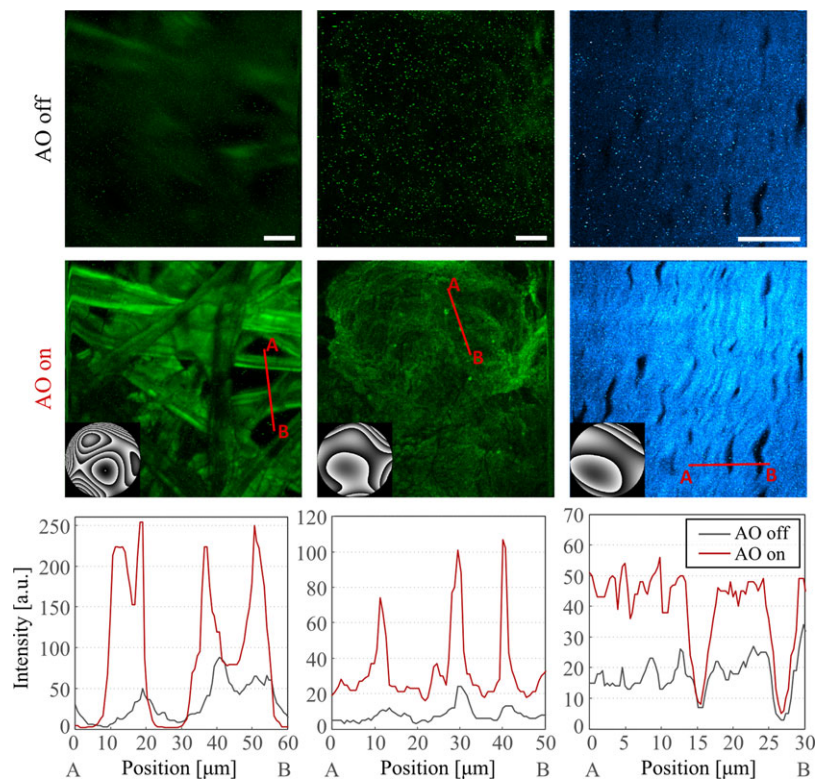
Fig. 4. TPEF and SHG images recorded before and after WA correction. Samples correspond to a piece of cellulose (140-μm depth, left panels), a nonstained human epiretinal membrane (50-μm depth, central panels) and a nonstained paraffin-embedded bovine cornea (40-μm depth, right panels). Intensity profiles (bottom plots) correspond to the red solid lines in the images. Insets are the WAs used for optimization. Bar length: 50 μm.
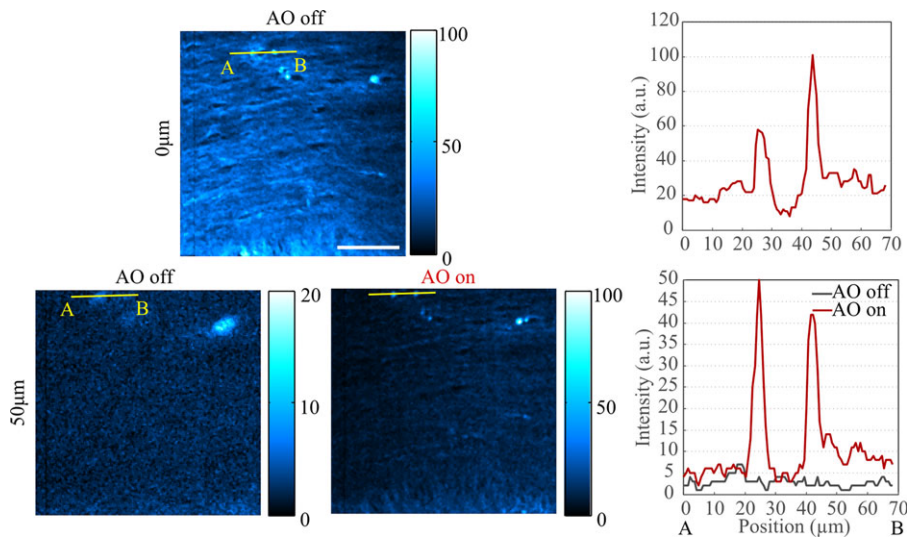

Fig. 5. Example of AO-MPM images showing the increase in contrast and resolution. Plots represent the intensity profiles of yellow lines in left panels. The sample corresponds to a rabbit cornea. Bar length: 50 μm.

applied to a larger one? In the following, the dependence of the WA map with the size of the imaged area will be explored.

The modal hill-climbing algorithm was run for different imaged areas in different samples and areas. For TPEF and SHG

signals, Figure 7 presents the improved images for two different imaged areas (S2 and S4, $180 \times 180 \ \mu m^2$ and $360 \times 360 \ \mu m^2$) together with the corresponding WA maps and Zernike distributions. As it can be seen, these WA maps (and
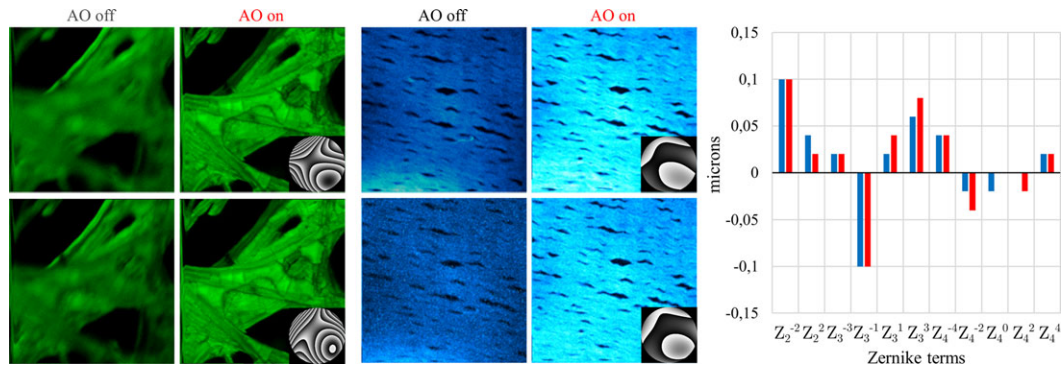
Fig. 6. Temporal stability and robustness of the AO procedure here proposed. Images were recorded 24 (TPEF, left panels) and 8 (SHG, right panels) hours apart. Samples are the same as those in Fig. 4. Image size: $180 \times 180 \ \mu m^2$. Depth locations: 100 and 30 μm, respectively. Right panel shows the corresponding 8-h apart Zernike terms for the improvement of SHG images.
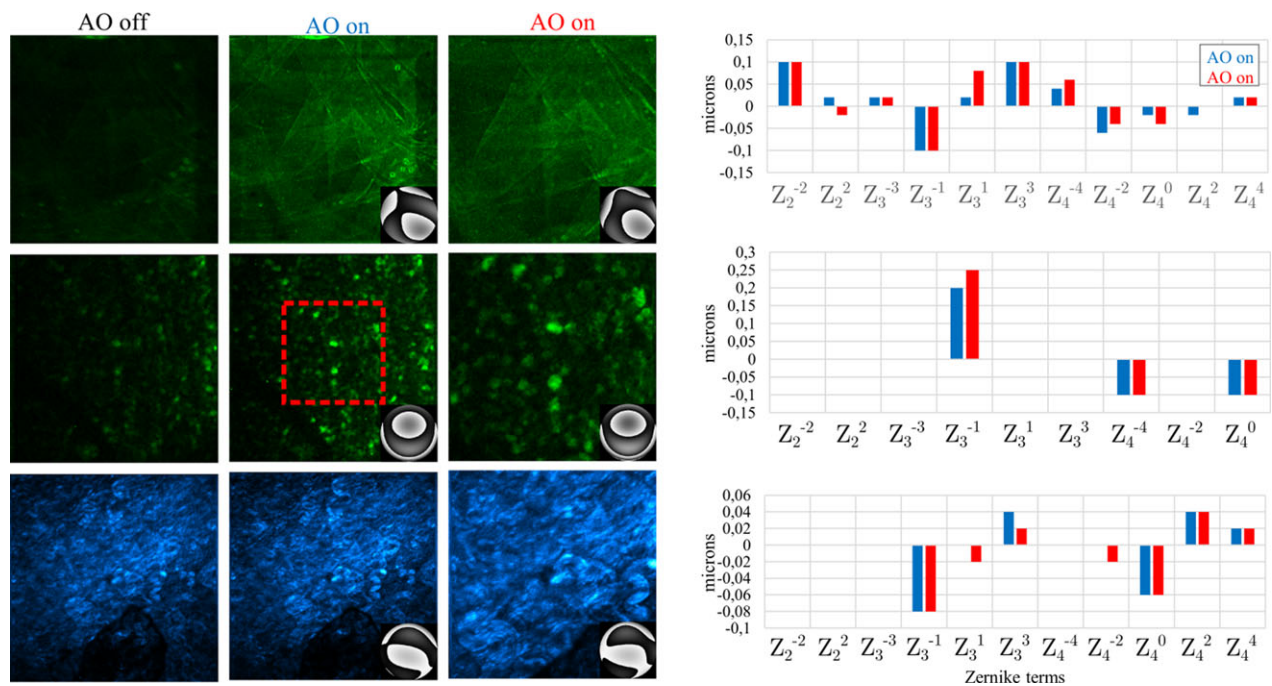

Fig. 7. Influence of the imaged area on the optimum WA maps for TPEF (human epiretinal membrane, top and rat retina ganglion cells, middle) and SHG (bovine sclera, bottom) images. Left and middle panels: $360 \times 360 \ \mu m^2$; right panels: $180 \times 180 \ \mu m^2$ (squared area in central image). The corresponding WA Zernike coefficients are shown on the right.

the corresponding Zernike terms) hardly changed between the two imaged areas, that is, the improved images are nearly independent of the size of the imaged area. This behaviour was similar for all samples and depth locations involved in the study.

Influence of the Zernike correction control sequence

The MPM images of the previous sections were obtained using the hill-climbing algorithm in the increasing-mode direction. For this condition, the AO optimization started by correcting the term Z_2^{-2} (45°-astigmatism). The effects of using the algorithm in the decreasing-mode direction have also been

investigated. Figure 8 shows the results in a piece of cellulose. For the decreasing-mode direction, the algorithm started with term Z_4^0 (spherical aberration) and the Zernike terms were included in the order indicated in the horizontal axis of the bottom plot. For both correction directions the final images were similar. Despite this, the WAs are different, although their RMS values did not differ much (1.05 and 0.94 μm, respectively).

The improvement (red line) corresponds to the ratio of the metric between each 'intermediate' image (i.e. when adding every Zernike term) and the uncorrected one. For the increasing-mode direction, 2nd-order terms (astigmatism) hardly had effect in image improvement. There is a ~2-fold
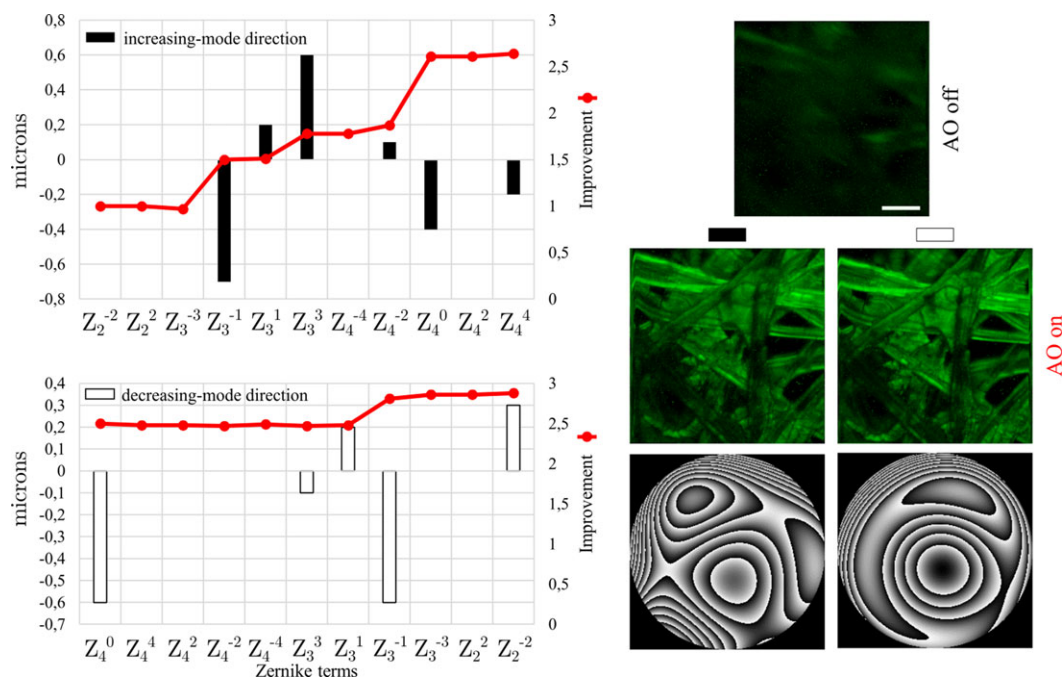
Fig. 8. Zernike terms for the increasing (black bars) and decreasing (white bars) directions. The red line corresponds to the image improvement when adding every Zernike term. The WA maps are shown for direct comparison. Images correspond to a 180-μm depth layer within a piece of cellulose. Bar length: 50 μm.
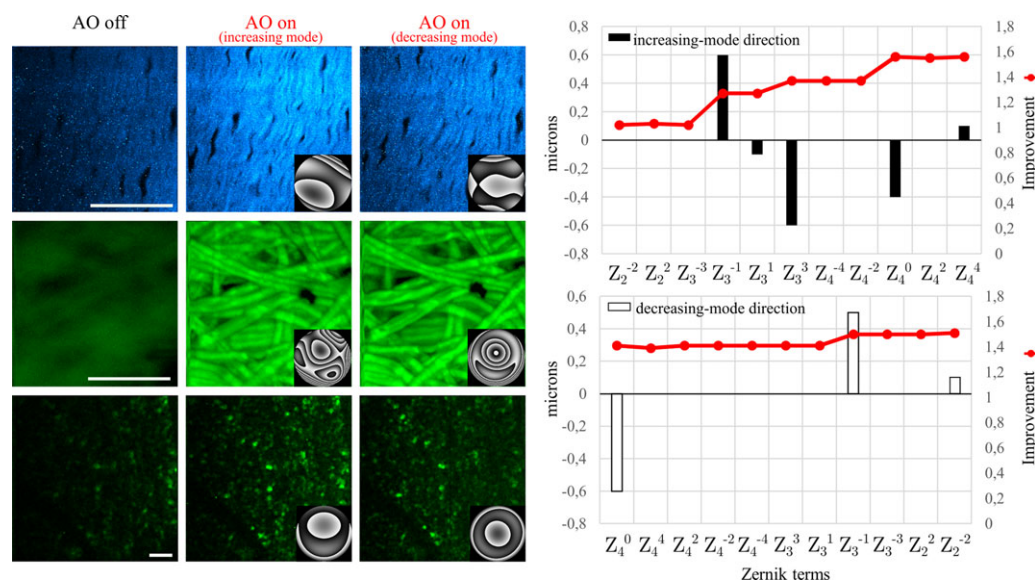

Fig. 9. Examples of MPM image improvement using the hill-climbing algorithm in the increasing and decreasing directions. Samples correspond to a paraffin-embedded bovine cornea (40-μm depth, upper panels), a piece of silk mesh (180-μm depth, middle panels) and the ganglion cell layer of a rat retina (30-μm depth, bottom panels). Bar length: 50 μm. The Zernike distribution plots on the right correspond to the silk mesh sample shown in the middle panels.

increase in improvement when adding 3rd-order terms (especially Z_3^{-1} and Z_3^{3}), and a ~2.5-fold increase when including 4th order ones (mainly spherical aberration).

In the decreasing-mode direction, most of the improvement was obtained when adding just the spherical aberration term (Z_4^{0}). The improvement did not change until the term Z_3^{-1} (vertical coma) was included, leading to an additional improvement. When adding the last term (Z_2^{-2}) a final improvement of ~2.5-fold compared to the original image was reached.
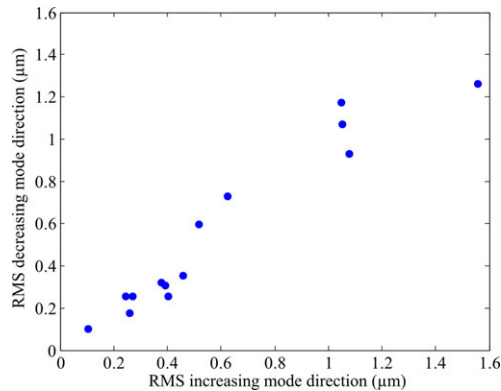
Fig. 10. Comparison of RMS values of the WAs obtained when the AO procedure was used in the increasing and decreasing Zernike-mode directions for different samples used in this work.

The comparison between the Zernike-mode sequences was also carried out in other samples. Figure 9 shows the results in a bovine cornea, a piece of silk mesh and a rat retina (ganglion cell layer). As also shown in Figure 8, WA maps differed but RMS values were similar. For a better understanding the Zernike distribution and the corresponding improvement are shown on the right of Figure 9.

For a number of samples involved in the present work and providing both TPEF and SHG signals, Figure 10 compares the RMS values of the WA maps in both correction directions. The data fit a significant linear relationship ($R = 0.92$; $p < 0.0001$).

Dominance of spherical aberration

Independent of the sample, the comparison between both Zernike-mode correction directions of the previous section has confirmed the dominance of the spherical aberration term (Hell *et al.*, 1993; Neil *et al.*, 2000; Sherman *et al.*, 2002; Lo *et al.*, 2005), especially when imaging layers placed at deeper locations. To better show this effect, Figure 11 presents examples of improved images in different specimens when correcting just the term Z_4^0 compared to those when the terms Z_3^3, Z_3^{-1} and Z_2^{-2} were also included.

These results confirm the benefit of just correcting the spherical aberration term, when it is dominant at certain depth positions within thick samples. This has been analysed in detail in a recent paper by these authors (Bueno *et al.*, 2014). Although the contribution of the spherical aberration term varies among samples and depth location, this was more than 60% (to the total RMS) in most samples analysed here.

Discussion

In this study a research multiphoton microscope has been modified to include an LCoS-SLM device, optimized for infrared light, as an AO element. We have

further explored the capabilities of an LCoS-SLM modulator for WA manipulation in order to improve multiphoton imaging. The dependence of the final improved image on the Zernike correction control sequence has been investigated, as well as the influence of the imaged area size.

Recently, LCoS-SLM modulators have successfully been used to improve multiphoton imaging at deep locations within the specimens (Ji *et al.*, 2010, 2012). Unlike deformable mirrors (with continuity constrains), these devices are able to reproduce discontinuous profiles and increase the effective stroke by means of phase wrapping. Whereas the number of independent elements in a deformable mirror is about 100, in an LCoS-SLM device this is 4 orders of magnitude higher. LCoS-SLM devices also provide much higher resolution than regular SLMs, what leads to enhanced accuracy for WA correction. WFSL approaches might also benefit from the use of LCoS-SLMs because their inherent fidelity also permits open-loop operation with no need of feedback for achieving the intended final WA.

One of the main drawbacks when using LCoS-SLM devices is the requirement of linearly polarized light. In MPM this would be important when analysing the effects of polarization on SHG imaging, however, that is irrelevant here due to the independence between aberrations and polarization (Bueno & Artal, 2001; Bueno *et al.*, 2006). Another important issue is the absorption coefficient. Depending on the angle of incidence, this might be higher than 50%. Its minimization is important to maximize the optical efficiency of the device and to minimize local heating (especially when using high-power mode-locked lasers). In MPM, when highly transparent samples providing TPEF signal are imaged, this is not important, however, in high-scattered samples providing SHG signal this absorption might be an additional factor limiting the optical penetration depth.

Because static samples are used in this work, the response velocity is not an issue. However, LCoS-SLM technology allows up to 60 Hz (Fernández *et al.*, 2009), values higher than those provided by regular liquid-crystal SLMs previously used in MPM. This increase in the response speed is due to a direct control of the local refractive index by a CMOS (Complementary Metal Oxide Semiconductor) sheet placed below the liquid crystal layer (Wang *et al.*, 2004). This may open new applications and possibilities in multiphoton imaging of dynamic samples where the recording time must be reduced and optimized (Olivier *et al.*, 2009; Wang *et al.*, 2014).

Several algorithms to perform image optimization in AO-MPM involving WFSL procedures can be found in the literature (Albert *et al.*, 2000; Neil *et al.*, 2000; Sherman *et al.*, 2002; Marsh *et al.*, 2003; Wright *et al.*, 2005; Débarre *et al.*, 2009; Zhou *et al.*, 2011; Tang *et al.*, 2012). Comparisons among different procedures are out of the scope of the present paper and can be found elsewhere (Wright *et al.*, 2005). The choice of an algorithm depends on the objective and requirements of the investigation. In general, it mainly depends on the 'best fit'
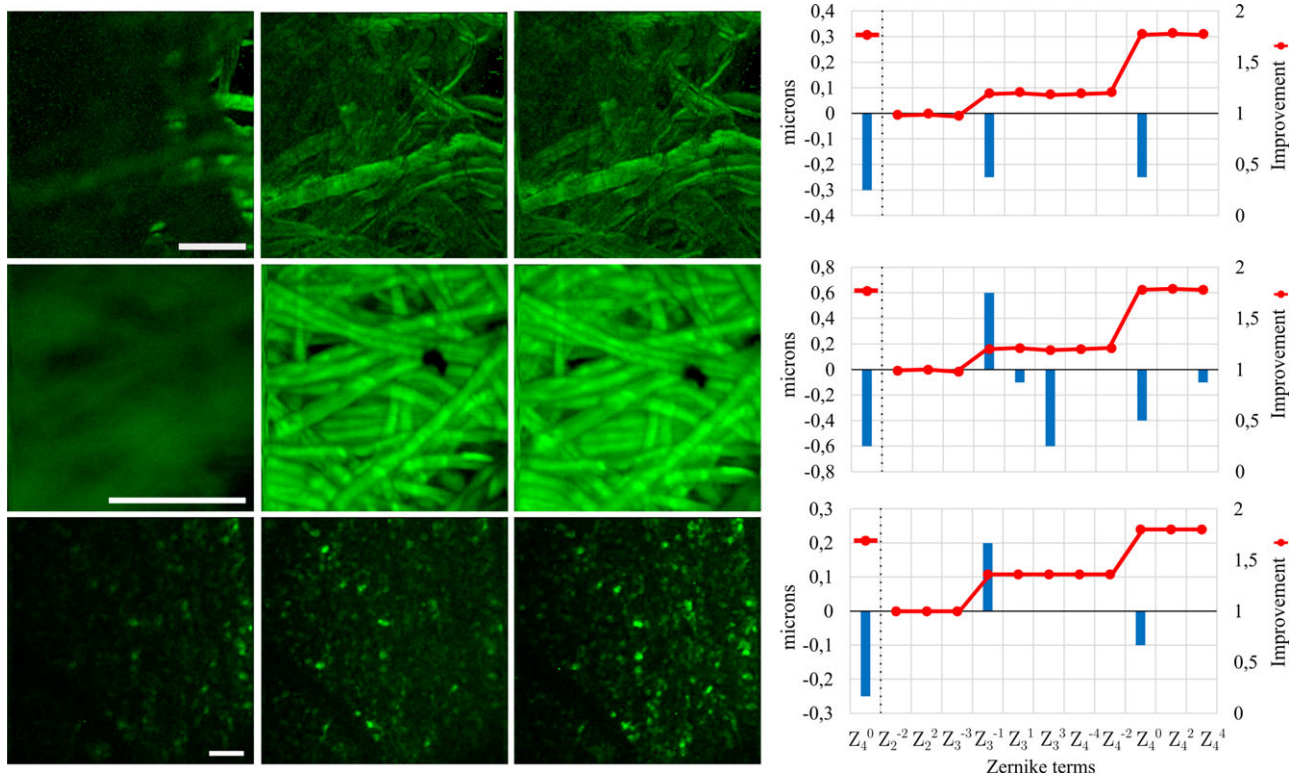
Fig. 11. Examples of MPM images showing the benefit of correcting the spherical aberration term. Samples correspond to a human epiretinal membrane (50-μm depth, top), a piece of silk mesh (80-μm depth, middle) and the ganglion cell layer of a rat retina (30-μm depth, bottom). Original image (left column); only spherical aberration corrected (middle column); spherical aberration, astigmatism, trefoil and coma corrected (right column). Images have the same intensity scale. Bar length: 50 μm. On the right, the Zernike distribution diagrams of each sample are shown. The first Zernike term of each diagram represents the benefit of only using spherical aberration correction and the corresponding improvement.

to the sample being imaged. Algorithms such as genetic (Man *et al.*, 1999) or simulated annealing (Kirkpatrick *et al.*, 1983) are inherently more complex and require many iterations and resources. If time is an issue, random search algorithms have been reported to be a good compromise between speed and image enhancement (Wright *et al.*, 2005; Lubeigt *et al.*, 2010). Alternatively, hill-climbing procedures offer less complexity and are appropriate for samples not prone to photo-bleaching of photo-toxicity (Marsh *et al.*, 2003) as the ones used here.

Moreover, iterative algorithms and correction strategies of WFSL systems have to be optimized to work efficiently. Nowadays, orthogonal functions such as Zernike polynomials are commonly used to effectively reduce the search space (Booth, 2006). This modal-based scheme in sequential use combined with hill-climbing algorithms has successfully been used in AO-MPM. More recently, the principle of the image-based modal aberration sensing method and its adaptation for 3D-resolved aberration measurements have been studied in detail (Zeng *et al.*, 2012).

A modal-based hill-climbing algorithm has been used here to improve images acquired with MPM. Although both, non-biological and biological samples were successfully tested,

our interest was mainly focused on ocular tissues. Results were shown to be reproducible with time. Because samples were static, this shows the temporal stability of the laser beam as previously reported by these authors (Bueno *et al.*, 2009).

The regular way of compensating aberration terms is starting with 2nd-order terms (astigmatism) and running them in the increasing-mode direction. Here we have compared the final WAs in both increasing and decreasing control sequences. Results for different samples show that the optimum WA depends on the chosen control sequence direction although the final improved images did not differ much. Despite WAs differ, for each particular specimen the total RMS values for both WAs were similar (Fig. 10). This indicates that different combinations of Zernike polynomials led to comparable improved images. To our knowledge, this has been described for the first time here.

Because Zernike polynomials are orthogonal, this result might be contradictory at this point. Obviously, a particular WA is described by a unique combination of Zernike terms. However, the idea here reported differs from this. At a certain depth location the specimen-induced aberrations (generally

understood as a total RMS value) reduce MPM efficiency. Our goal has been to test if the image improvement can be reached by using different combinations of Zernike terms. It has been shown that different combinations led to similar improved images attending to a particular metric. This fact is not directly related to the mathematical properties of the Zernike terms but with the image improvement itself. In fact, it was found that the different compensations providing similar RMS values led to similar final images. This means that the plane-to-plane WA correction is not based on an exclusive WA map but in the compensation of a total RMS representing a 'certain amount of aberration'.

For most samples, the decreasing-mode direction provided the spherical aberration as the dominant term, especially at deeper locations, being the influence of the rest of terms minor. On the contrary, in the increasing-mode direction different terms contribute to get the best quality image. These results corroborate the fact that the spherical aberration itself might significantly contribute to enhance the images (mainly at deeper locations). A compensation of this aberration term using AO non-linear tomography would help to improve multiphoton images in an easy and 'fast' way, as recently reported by these authors (Bueno *et al.*, 2014).

In AO-MPM it is also important to consider the variations of the aberrations across the field of view. If for a given depth location, a larger (or smaller) area is imaged, the required WA to optimize the image might be different (Schwertner *et al.*, 2004). Lateral scan aberrations can also become significant in microscopy and generally increase with the scan angle (Marsh *et al.*, 2003). Simmonds and Booth (Simmonds & Booth, 2013) have recently reported a model of spatially variant aberration correction through multiconjugate adaptive optics. They claimed that those aberrations can be partially compensated by correcting for the entire field of view. Moreover, Zheng *et al.* (2013) have reported a phase retrieval-based procedure to experimentally recover the spatially varying WAs in wide-field imaging systems. In this paper, different fields of view were imaged and optimized in a number of samples (largest imaged area: $360 \times 360 \ \mu m^2$). It was found that for a certain depth location within a sample, the WAs were similar for all imaged areas. This is consistent with previous results (Aviles-Espinosa *et al.*, 2011).

The reason for this might be that the samples here used do not present so much variation across the field of view (especially ocular tissues). Because slower scan rates are expected when imaging a bigger area, the current results lead to the fact that an improved MPM image of a bigger area can be achieved, by correcting only over a particular smaller region (imaged in a shorter time). This is of interest for future applications of the reported procedure to living eyes, where the recording time might be an issue.

In conclusion, an LCoS–SLM device has been implemented into a multiphoton microscope to enhance the contrast and resolution of images without noticeable photo-damage. The microscope was set to use an in-air objective and a backscattered configuration. A modal hill-climbing algorithm has been developed to successfully correct for the aberrations in specimens providing both TPEF and SHG signal. A comparison of optimum images given by two different Zernike-mode control sequences has been reported. This image improvement might allow a better visualization of ocular tissues, in particular those suffering from some pathology with features located at deeper locations. The main drawback of the reported method is the number of iterations used (although these can be reduced; Débarre *et al.*, 2007). This would limit its use with dynamic samples. The present experimental system is not optimized for speed but this will be improved when moved to *in vivo* imaging in the near future. As recently reported (Bonora & Zawadzki, 2013), the combination of modal correction of low-order aberrations with a stochastic parallel gradient descent algorithm for high-order aberrations (Hofer *et al.*, 2011) might improve the performance when dynamic measurements are involved.

Acknowledgement

References

Albert, O., Sherman, L., Mourou, G., Norris, T.B. & Vdovin, G. (2000) Smart microscope: an adaptive optics learning system for aberration correction in multiphoton confocal microscopy. *Opt. Lett.* **25**(1), 52–54.

Aviles-Espinosa, R., Olarte, O.E., Porcar-Guezenec, R. *et al.* (2011) Measurement and correction of in vivo sample aberrations employing a nonlinear guide-star in two-photon excited fluorescence microscopy. *Biomed. Opt. Express* **2**(11), 3135–3149.

Bonora, S. & Zawadzki, R.J. (2013) Wavefront sensorless modal deformable mirror correction in adaptive optics: optical coherence tomography. *Opt. Lett.* **38**(22), 4801–4804.

Booth, M.J. (2006) Wave front sensor-less adaptive optics: a model-based approach using sphere packings. *Opt. Express* **14**(4), 1339–1352.

Booth, M.J. & Wilson, T. (2001) Refractive-index-mismatch induced aberrations in single-photon and two-photon microscopy and the use of aberration correction. *J. Biomed. Opt.* **6**(3), 266–272.

Bueno, J.M. & Artal, P. (2001) Polarization and retinal image quality estimates in the human eye. *JOSA A* **18**(3), 489–496.

Bueno, J. M., Berrio, E. & Artal, P. (2006) Corneal polarimetry after LASIK refractive surgery. *J. Biomed. Opt.* **11**(1), 14001.

Bueno, J.M., Gualda, E.J. & Artal, P. (2010) Adaptive optics multiphoton microscopy to study ex vivo ocular tissues. *J. Biomed. Opt.* **15**(6), 66004.

Bueno, J.M., Gualda, E.J. & Artal, P. (2011) Analysis of corneal stroma organization with wavefront optimized nonlinear microscopy. *Cornea* **30**(6), 692–701.

Bueno, J.M., Gualda, E.J., Giakoumaki, A., Pérez-Merino, P., Marcos, S. & Artal, P. (2011) Multiphoton microscopy of ex vivo corneas after collagen cross-linking. *Invest. Ophthalmol. Vis. Sci.* **52**(8), 5325–5331.

Bueno, J.M., Skorsetz, M., Palacios, R., Gualda, E.J. & Artal, P. (2014) Multiphoton imaging microscopy at deeper layers with adaptive optics control of spherical aberration. *J. Biomed. Opt.* **19**(1), 11007.

Bueno, J.M., Vohnsen, B., Roso, L. & Artal, P. (2009) Temporal wavefront stability of an ultrafast high-power laser beam. *Appl. Opt.* **48**(4), 770–777.

Campagnola, P.J., Lewis, A., Loew, L.M., Clark, H.A. & Mohler, W.A. (2001) Second-harmonic imaging microscopy of living cells. *J. Biomed. Opt.* **6**(3), 277–286.

Débarre, D., Booth, M.J. & Wilson, T. (2007) Image based adaptive optics through optimisation of low spatial frequencies. *Opt. Express* **15**(13), 8176–8190.

Débarre, D., Botcherby, E.J., Watanabe, T., Srinivas, S., Booth, M.J. & Wilson, T. (2009) Image-based adaptive optics for two-photon microscopy. *Opt. Lett.* **34**(16), 2495–2497.

Denk, W., Strickler, J.H. & Webb, W.W. (1990) Two-photon laser scanning fluorescence microscopy. *Science* **248**(4951), 73–76.

Fernández, E.J., Prieto, P.M. & Artal, P. (2009) Wave-aberration control with a liquid crystal on silicon (LCOS) spatial phase modulator. *Opt. Express* **17**(13), 11013–11025.

Girkin, J.M., Poland, S. & Wright, A.J. (2009) Adaptive optics for deeper imaging of biological samples. *Curr. Opin. Biotechnol.* **20**(1), 106–110.

Han, M., Giese, G. & Bille, J. (2005) Second harmonic generation imaging of collagen fibrils in cornea and sclera. *Opt. Express* **13**(15), 5791–5797.

Hell, S., Reiner, G., Cremer, C. & Stelzer, E.H.K. (1993) Aberrations in confocal fluorescence microscopy induced by mismatches in refractive index. *J. Microsc.* **169**(3), 391–405.

Hofer, H., Sredar, N., Queener, H., Li, C. & Porter, J. (2011) Wavefront sensorless adaptive optics ophthalmoscopy in the human eye. *Opt. Express* **19**(15), 14160–14171.

Hovhannisyan, V.A., Su, P.-J. & Dong, C.Y. (2008) Characterization of optical-aberration-induced lateral and axial image inhomogeneity in multiphoton microscopy. *J. Biomed. Opt.* **13**(4), 44023.

Jesacher, A., Thayil, A., Grieve, K., Débarre, D., Watanabe, T., Wilson, T., Srinivas, S. & Booth, M. (2009) Adaptive harmonic generation microscopy of mammalian embryos. *Opt. Lett.* **34**(20), 3154–3156.

Ji, N., Milkie, D.E. & Betzig, E. (2010) Adaptive optics via pupil segmentation for high-resolution imaging in biological tissues. *Nat. Methods* **7**(2), 141–147.

Ji, N., Sato, T.R. & Betzig, E. (2012) Characterization and adaptive optical correction of aberrations during in vivo imaging in the mouse cortex. *Proc. Natl. Acad. Sci* **109**(1), 22–27.

Kirkpatrick, S., Gelatt, C.D. & Vecchi, M.P. (1983) Optimization by simmulated annealing. *Science* **220**(4598), 671–680.

Leray, A., Lillis, K. & Mertz, J. (2008) Enhanced background rejection in thick tissue with differential-aberration two-photon microscopy. *Biophys. J.* **94**(4), 1449–1458.

Leray, A. & Mertz, J. (2006) Rejection of two-photon fluorescence background in thick tissue by differential aberration imaging. *Opt. Express* **14**(10), 510–565.

Lo, W., Lin, S.-J., Jee, S.-H., Dong, C.-Y. & Sun, Y. (2005) Spherical aberration correction in multiphoton fluorescence imaging using objective correction collar. *J. Biomed. Opt.* **10**(3), 34006–340065.

Lubeigt, W., Poland, S.P., Valentine, G.J., Wright, A.J., Girkin, J.M. & Burns, D. (2010) Search-based active optic systems for aberration correction in time-independent applications. *Appl. Opt.* **49**(3), 307–314.

Man, K.-F., Tang, K.S. & Kwong, S. (1999) *Genetic Algorithms: Concepts and Designs (Advanced Textbooks in Control and Signal Processing)*. Springer-Verlag, London.

Marsh, P.N., Burns, D. & Girkin, J.M. (2003) Practical implementation of adaptive optics in multiphoton microscopy. *Opt. Express* **11**(10), 1123–1130.

Muller, R.A. & Buffington, A. (1974) Real-time correction of atmospherically degraded telescope images through image sharpening. *JOSA* **64**(9), 1200–1210.

Neil, M.A.A., Juskaitis, R., Booth, M.J., Wilson, T., Tanaka, T., Kawata, S. & Juškaitis, R. (2000) Adaptive aberration correction in a two-photon microscope. *J. Microsc.* **200**(2), 105–108.

Olivier, N., Débarre, D. & Beaurepaire, E. (2009) Dynamic aberration correction for multiharmonic microscopy. *Opt. Lett.* **34**(20), 3145–3147.

Rueckel, M., Mack-Bucher, J.A. & Denk, W. (2006) Adaptive wavefront correction in two-photon microscopy using coherence-gated wavefront sensing. *Proc. Natl. Acad. Sci.* **103**(46), 17137–17142.

Schwertner, M., Booth, M.J., Neil, M.A.A. & Wilson, T. (2004) Measurement of specimen-induced aberrations of biological samples using phase stepping interferometry. *J. Microsc.* **213**(1), 11–19.

Shao, Y., Qin, W., Liu, H., Qu, J., Peng, X., Niu, H. & Gao, B.Z. (2012) Multifocal multiphoton microscopy based on a spatial light modulator. *Appl. Phys. B* **107**(3), 653–657.

Sherman, L., Ye, J.Y., Albert, O. & Norris, T.B. (2002) Adaptive correction of depth-induced aberrations in multiphoton scanning microscopy using a deformable mirror. *J. Microsc.* **206**(1), 65–71.

Simmonds, R.D. & Booth, M.J. (2013) Modelling of multi-conjugate adaptive optics for spatially variant aberrations in microscopy. *J. Opt.* **15**(9), 94010.

Tang, J., Germain, R.N. & Cui, M. (2012) Superpenetration optical microscopy by iterative multiphoton adaptive compensation technique. *Proc. Natl. Acad. Sci.* **109**(22), 8434–8439.

Tao, X., Norton, A., Kissel, M., Azucena, O. & Kubby, J. (2013) Adaptive optical two-photon microscopy using autofluorescent guide stars. *Opt. Lett.* **38**(23), 5075–5078.

Wang, K., Milkie, D.E., Saxena, A., Engerer, P., Misgeld, T., Bronner, M.E., Mumm, J. & Betzig, E. (2014) Rapid adaptive optical recovery of optimal resolution over large volumes. *Nat. Methods* **11**(6), 625–628.

Wang, X., Pouch, J., Anderson, J.E., Bos, P.J., Miranda, F. & Wang, B. (2004) Performance evaluation of a liquid-crystal-on-silicon spatial light modulator. *Opt. Eng.* **43**(11), 2769–2774.

Wright, A.J., Burns, D., Patterson, B.A., Poland, S.P., Valentine, G.J. & Girkin, J.M. (2005) Exploration of the optimisation algorithms used in the implementation of adaptive optics in confocal and multiphoton microscopy. *Microsc. Res. Tech.* **67**(1), 36–44.

Zeng, J., Mahou, P., Schanne-Klein, M.-C., Débarre, D. & Beaurepaire, E. (2012) 3D resolved mapping of optical aberrations in thick tissues. *Biomed. Opt. Express* **3**(8), 1898–1913.

Zheng, G., Ou, X., Horstmeyer, R. & Yang, C. (2013) Characterization of spatially varying aberrations for wide field-of-view microscopy. *Opt. Express* **21**(13), 15131–15143.

Zhou, Y., Bifano, T. & Lin, C. (2011) Adaptive optics two-photon scanning laser fluorescence microscopy. *SPIE MOEMS-MEMS*, 79310H–79310H.